

Numerical study of the effect of mass of the background gas on the lateral interactions of two plasma plumes at high pressure

Sharad K. Yadav¹† and R. K. Singh² §

¹Department of Physics, Indian Institute of Science (IISc.), Bangalore 560012, Karnataka, India

²Institute for Plasma Research (IPR), Gandhinagar 382428, India

Abstract. The characteristic of the lateral interaction of two plasma plumes in argon *Ar* background gas at high pressures was reported in recent publication [Yadav *et. al.*, J. Phys. D: Appl. Phys. **50**, 053421 (2017)]. Further we have investigated the interaction characteristics of plumes in *He*, *Ne*, *Ar* and *Xe* background gases to see the effect of mass on the interaction. The present work illustrate the applicability of the present model for theoretical understanding of dynamics, structure, density variation, shock wave formations and their interactions of two propagating plasma plumes in a wide range of ambient conditions. The formation of interaction region, geometrical shape and strength of the shock fronts and subsequent regular and Mach reflections in accordance with the nature and pressure of ambient gas are successfully captured in the simulations. The observed results are supported by the reported experimental observations under identical conditions.

Keywords: Fluid simulation, Shock wave, Laser-blow-off (LBO), Plasma plume.

† sharadyadav@iisc.ac.in;sharadky@gmail.com

§ rajesh@ipr.res.in

1. Introduction

Laser interaction with matter and subsequent evolution of target material as a form of plasma plume has a variety of applications in many areas such as pulse laser deposition, nano-particles/clusters formation, material processing, elemental analysis, lithography, atmospheric plasma and plasma diagnostics [1, 2, 3, 4, 5, 6, 7]. Many parameters such as laser wavelength and energy density, properties of material (e.g. thermal conductivity, heat capacity, density) and also the reflectivity and absorption of material collectively govern the plasma formation. Hence the basic mechanism of the formation and the evolution of laser produced plasma plume is a complex process and its theoretical understanding continues to be a challenging task.

Apart from the extensive research on single laser plasma plume, the interaction between the plasma plumes, also known as colliding plasmas [8] has been subject of great interest because of its applications in laser ion source, inertial confinement fusion (ICF), and laboratory simulation and modelling of astrophysical plasma phenomena [9, 10, 11, 12, 13, 14]. When the plasma plumes interact under certain conditions, an interaction region or plasma jet like structure is formed [15]. The dynamics and plasma parameters of this additional jet like structure is depend on the geometry of the interaction and plasma parameters of interacting plumes (seed plumes). Several experiments have been done to manipulate the induced plasma jet like structure by using the different interaction geometry, e.g. head-on collisions, angular and lateral interactions where the seed plasma plumes are generated with wide range of laser intensities [16, 17, 18, 19, 20, 21]. The increasing interest in colliding plasmas induced interaction reason is largely due to its better control of the plasma parameters and geometrical shape in accordance with its applications.

Plasma jet produced by energetic colliding plasmas immersed as a important tool for laboratory scaled model of various astrophysical phenomenon [12, 13, 14]. Camps *et. al.* [22] utilize the colliding plasma to produce an aggregate-free materials source. Y. Hirooka *et. al.* [23] study the Aerosol formation and hydrogen co-deposition by colliding ablation plasma plumes from plasma facing element. Further colliding plasmas is used to understand the stagnation on hohlraum axis and capsule implosions in ICF [10, 11]. In addition to the widely explored the collision between the conventional laser produced plasmas, recently several experiments have been conducted to understand the interaction between the Laser-Blow-Off (LBO) of the thin film [24, 25]. Due to the difference in ablation mechanism, the thermal history, composition and evolution of LBO plume is significantly different from plasma plume produced by bulk solid target [26]. Since the major constituents of LBO plume is neutral species and therefore the interaction between LBO plasmas can be used to generate the directed beam of neutral species for tokomak plasma diagnostics [27, 28].

In spite of extensive application oriented work on the laser produced colliding plasma plumes, its theoretical understanding are scarce in the literature. Also the interaction between the plasma plumes in presence of ambient gas is more complex in

comparison to the case of vacuum because of the presence of shock front ahead of the plasma plume [29, 30, 31]. In presence of shock front, the interaction between the plumes is governed by shock-shock collision and its reflection [24]. The understanding of colliding shock is important, especially in probing the astronomical object in laboratory scale [12, 13].

Recently, we have simulated the lateral interactions between two spatially separated LBO plasma plumes in the presence of argon ambient [32]. In this approach, continuity, momentum and the energy equations of ablated material are solved numerically in two dimension [32, 33]. In this numerical study we showed the formation of shock waves and their interactions in argon ambient which is in good agreement with experimental observations [32]. Since evolution of the plasma plume and also the geometrical shape and strength of the shock wave is depends on the on the pressure and mass of the ambient gas; which collectively determine the dynamics and structure formation of the induced interaction region. Therefore we are motivated to look more closely the interactions between the LBO plumes in wide range of ambient environment.

In extension of our earlier work [32], here we report the two dimensional numerical simulation of interaction of LBO plume in *He*, *Ne*, *Ar* and *Xe* background. These background gases are chosen because of large difference in their atomic masses and the physical parameters.

2. Modeling of Plasma Plumes and Numerical Simulation

2.1. Basic fluid equations:

We modeled the time evolution of plasma-plume in the ambient gas using basic fluid equations that include mass, momentum and energy equations.

Mass equation:

$$\frac{\partial \rho}{\partial t} = -\vec{\nabla} \cdot (\rho \vec{u}) \quad (1)$$

In eq. (1) ρ is the mass density of whole system i.e. $\rho = \rho_v + \rho_b$; ρ_v is the plume density (also known as vapor density) and ρ_b is the background gas density; \vec{u} is the flow velocity.

Mass equation (only for the plasma plume):

$$\frac{\partial \rho_v}{\partial t} = -\vec{\nabla} \cdot (\rho_v \vec{u}) + \vec{\nabla} \cdot (\rho D_{mix} \vec{\nabla} \Omega_v) \quad (2)$$

In which D_{mix} is the binary diffusion coefficient expressed as $D_{mix} = \frac{2}{3} \left(\frac{k}{\pi} \right)^{3/2} \left(\frac{1}{2m_v} + \frac{1}{2m_b} \right)^{\frac{1}{2}} \frac{T^{\frac{3}{2}}}{p \left(\frac{d_v + d_b}{2} \right)^2}$; d_v and d_b are the size of the vapor and background gas species respectively; pressure p and temperature T are related to each other by the relation $p = \rho_v kT/m_v + \rho_b kT/m_b$; m_v is the mass of the vapor plume species and m_b is the mass of the background gas species. Ω_v is the vapor mass density fraction i.e. $\Omega_v = \rho_v/\rho$.

Momentum equation:

$$\frac{\partial \rho \vec{u}}{\partial t} = -\vec{\nabla} \cdot (\rho \vec{u} \vec{u}) - \vec{\nabla} p + \vec{\nabla} \cdot \bar{\bar{Q}} \quad (3)$$

Energy equation:

$$\frac{\partial E}{\partial t} = -\vec{\nabla} \cdot (E \vec{u}) - p \vec{\nabla} \cdot \vec{u} - \vec{\nabla} \cdot \vec{q} + \bar{\bar{Q}} : \vec{\nabla} \vec{u} + \vec{\nabla} \cdot [(E_v - E_b) \rho D_{mix} \vec{\nabla} \Omega] \quad (4)$$

We consider the transfer of momentum due to the symmetric viscous stress tensor $\bar{\bar{Q}}$ defined as:

$$\bar{\bar{Q}} = \eta_{mix} \left[\left\{ \vec{\nabla} \vec{v} + (\vec{\nabla} \vec{v})' \right\} - \frac{2}{3} (\vec{\nabla} \cdot \vec{v}) \bar{\bar{I}} \right] \quad (5)$$

where $(\vec{\nabla} \vec{v})'$ represents the transpose of the tensor $\vec{\nabla} \vec{v}$. The viscosity η_{mix} of the binary mixture is determined using semi-empirical formula of Wilke provided in Ref. [34] as.

$$\eta_{mix} = \sum_i \frac{f_i \eta_i}{\sum_j f_j \Phi_{ij}} \quad (6)$$

The suffixes i and j are to be summed over the two species of the vapor v and background gas b for the case of binary gas mixture. Here f_i and η_i are the number density fraction and the viscosity respectively for the i^{th} species and Φ_{ij} is a dimensionless number given by the expression below.

$$\Phi_{ij} = \frac{1}{\sqrt{8}} \left(1 + \frac{m_i}{m_j} \right)^{-1/2} \left[1 + \left(\frac{\eta_i}{\eta_j} \right)^{1/2} \left(\frac{m_j}{m_i} \right)^{1/4} \right]^2 \quad (7)$$

The viscosity corresponding to the individual species is calculated from the kinetic theory of the gas,

$$\eta_i = \frac{1}{\pi d_i^2} \sqrt{\frac{m_i k T}{\pi}} \quad (8)$$

where E in eq.(4) is the total internal energy *i.e.* $E = \frac{3}{2} \left(\frac{\rho_v}{m_v} + \frac{\rho_b}{m_b} \right) k T$. In energy equation the transfer of energy between vapor and background gas species are considered due to the heat flux \vec{q} , stress tensor $\bar{\bar{Q}}$ and also due to the different value of energy contents in the vapor and background gas species. The quantity \vec{q} in Eq. (4) is the heat flux defined as, $\vec{q} = -k_{mix} \vec{\nabla} T$ where k_{mix} is the thermal conductivity of the binary gas mixture. The thermal conductivity of individual species is determined using the semi empirical formulation and this is given by the following expression:

$$k_i = \frac{1}{d_i^2} \sqrt{\frac{k^3 T}{\pi^3 m_i}} \quad (9)$$

2.2. Simulation, melting and vaporization of the target material:

Experimental study suggest that the time evolution of plasma plume in the background gas is the axis symmetry phenomena. So to avoid the mathematical complexity and

also the computational expenses required in order to perform the numerical study in three-dimension (3D), we carry out simulation in two-dimension (2D). Therefore we solved Eqs. (1 – 4) numerically in two-dimension (2D) using the flux corrected scheme of Boris *et. al.* [36].

In figure 1 we displayed the schematic diagram of 2D computational domain and boundary conditions imposed on the boundaries. We used solid wall and inflow boundary conditions for the boundary. In solid wall boundary conditions the velocity component normal to boundary is taken to be zero and also the gradient of the quantities pressure p , transverse component of velocity v_y and density ρ_v normal to the boundary are set to zero. In inflow boundary condition the normal component of the flow velocity v_x at the boundary should be constant, pressure and density is also constant at the boundary. Boundaries assigned by the numbers 1, 3, 4, 5, 6, 7 is kept at the solid wall boundary condition through the simulation. Region 2 are the locations where the plasma plume will be produced throughout the ablation process. So region two is kept at inflow boundary boundary condition during the ablation process. When the plumes are completely formed in the computational space, region 2 is switched with the solid wall boundary condition. Time required in the ablation process is computed using the formula, $t_{vap} = \frac{M_a}{\rho_v v_v A}$ where M_a is the mass of the ablated thin film which can be evaluated from the density of the film, its thickness and the cross-section area A of the focused laser spot.

Surface temperature T_s of the ablated material is calculated by equating the incident laser energy with the energy required for the melting of the target material and further its vaporization.

$$F_L A (1 - R) = M_A c_S (T_{boi} - T_r) + (T_s - T_{boi}) + M_A \lambda_e \quad (10)$$

or,

$$T_s = T_r + \frac{F_L A (1 - R) - M_A \lambda_e}{c_s M_A} \quad (11)$$

Where F_L is the laser fluence, A is the spot size of the laser, R is the reflectivity, c_s is the specific heat of material, λ_e is the latent heat of evaporation, T_{boi} is the boiling temperature and T_r is the room temperature. Further we use T_s for the computation of the surface pressure p_s using the the Clausius-Clapeyron equation [35],

$$p_s = p_0 \exp \left[\frac{M_A \Delta H_{vap}}{k_b} \left\{ \frac{1}{T_{boi}} - \frac{1}{T_s} \right\} \right] \quad (12)$$

Here T_{boi} is normal boiling temperature at standard pressure p_0 and ΔH_{vap} is the vaporization enthalpy at temperature of T_{boi} at standard pressure p_0 . The ablated material from the surface moves towards the ambient gas and the Knudsen layer is formed whose thickness is of the order of a few mean free paths. In the Knudsen layer there is a drop in both temperature as well as the pressure of the ablated material by the following factors:

$$T = 0.67 T_s; p = 0.21 p_s \quad (13)$$

Our computational domain starts after this Knudsen layer. Therefore we use Eq. (13) for the estimation of the temperature T and pressure p of the inflowing ablated material. These then decide density ρ_v of the incoming ablated material (used in Eq. (14)) from the ideal gas law. The velocity with which the vapor enters the ambient medium is approximated by the velocity of sound.

$$v_v = \left(\frac{\gamma k_b T}{m_v} \right)^{1/2} \quad (14)$$

The values of the physical properties of the carbon target material used in the simulation

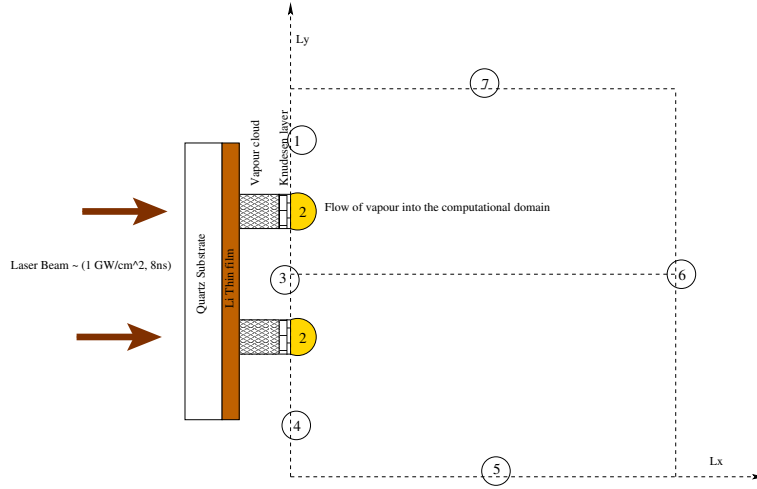


Figure 1. Schematic diagram of 2D computational space in the xy plane; each of sides L_x and L_y are $2.5m$ span in the region from 0 to 2.5; we also display the relevant components used in the experiment though not directly involved in the simulation. Numbers inside the circle represent the different boundary conditions imposed at boundaries. These boundary conditions are as follows: ① $v_x = 0, \frac{\partial p}{\partial x} = \frac{\partial \rho}{\partial x} = \frac{\partial v_y}{\partial x} = 0$; ② $(t > t_{vap}) v_y = 0, p = p, \rho = \rho_v, v_x = v_v$; ③ $(t < t_{vap}) v_x = 0, \frac{\partial p}{\partial x} = \frac{\partial \rho}{\partial x} = \frac{\partial v_y}{\partial x} = 0$; ④ $v_x = 0; \frac{\partial p}{\partial x} = \frac{\partial \rho}{\partial x} = \frac{\partial v_y}{\partial x} = 0$; ⑤ $v_y = 0; \frac{\partial p}{\partial y} = \frac{\partial \rho}{\partial y} = \frac{\partial v_x}{\partial y} = 0$; ⑥ $v_x = 0; \frac{\partial p}{\partial x} = \frac{\partial \rho}{\partial x} = \frac{\partial v_y}{\partial x} = 0$; ⑦ $v_y = 0; \frac{\partial p}{\partial y} = \frac{\partial \rho}{\partial y} = \frac{\partial v_x}{\partial y} = 0$; Note that this figure is borrowed from our earlier work [32]

are as follows: $\rho_s = 1.4 \text{ g/cm}^3$; $T_{boi} = 4492^\circ\text{C}$; $c_s = 710 \text{ J/kg.K}$; $\lambda_e = 356 \text{ kJ/mol}$; $R = 0.5$, where ρ_s , T_{boi} , c_s , λ_e and R are respectively, bulk density, boiling point, specific heat, latent evaporation and reflectivity. The initial values of various parameters/quantities (required in the simulation) are computed using formula given in this section. The value of these physical parameters/quantities are as follows: temperature $T = 9.35 \times 10^4 \text{ K}$, pressure $p = 1.25 \times 10^7 \text{ Pa}$, density $\rho = 1.93 \text{ kg/m}^3$, velocity $v_v = 9.53 \times 10^3 \text{ m/s}$, vapor-flux $J = 1.84 \times 10^4 \text{ kg/m}^2.s$ and vaporization-time $t_{vap} = 3.8 \times 10^8 \text{ s}$.

3. Numerical Results and Discussion

We solved numerically Eqs. (1 – 4) for the study of the lateral interaction of two plasmaplumes in the presence of the various background gases. The background gases considered in the simulations are *He*, *Ne*, *Ar* and *Xe*. The separation between the plumes are considered $\sim 5mm$. The simulations are performed at two background pressures 1 and 3 *mbar* in the all cases.

Time evolution of the plumes at 1 *mbar* and 3 *mbar* background pressure in the presence of *He*, *Ne*, *Ar* and *Xe* are shown in Figures 2 and 3 respectively. Visible examination of the images in figure 2 clearly show the effect of mass of ambient gas on the dynamics of expanding plasma plumes. In case of lighter gas i.e. *He*, plasma plume expands linearly up to the considered time delay as similar to the expansion in vacuum. An additional fable semicircular structure appeared ahead of the plasma plume at time delay 508 *ns* which is attributed as shock front. Here, the sound wave velocity c_s in *He*, *Ne*, *Ar* and *Xe* are 10.22×10^2 *m/s*, 4.54×10^2 *m/s*, 3.23×10^2 *m/s* and 1.78×10^2 *m/s* respectively. Using relation (14) the estimated initial plume velocity is $\sim 1.12 \times 10^4$ *m/s*, which is much higher than the sound wave velocity in the considered medium. This satisfy the strong shock condition especially in heavier background gas. The shock fronts are different to each other in terms of size and intensity depending upon background gas used in the simulation. In case of *Ne*, shock front is clearly visible at 304 *ns* whereas it appears further earlier ~ 208 *ns* in the case of heavier ambient gases that is *Ar* and *Xe*. Also the shock front is strengthened and more intense in heavier background gas.

In order to further study of the dynamics of plasma induced shock waves, axial-plume-dimensions (distance from the target to shock front) are analysed as a function of time. Figure 5 shows the variation of the distance of the shock-front from the target (also known as shock-distance) with time for all the cases of the simulation of the ambient gas performed at 1 *mbar* pressure.

In all cases we observe that initially for a very short time period, plasma plume expands linearly in all background gases. After a certain time delayed depending upon the mass of the background gas, the expansion of the plume is deviated from the linear expansion and it follows $\sim t^{0.4}$ dependence (see figure 5). It is clearly visible in our simulation as shown in figure 2, 3 and 4 where in heavier background gas shock wave initiated earlier in comparison to that observed in the case of the simulation of lighter-gas at a fixed background pressure. Delayed non-linear expansion behavior and its dependence on the mass of the background gas is in agreement with the blast wave model that describe the expansion of the massive-shock present in the gases system. In figure 6 we observe that shock front appears roughly at 0.012 *m*, 0.009 *m*, 0.008 *m* and 0.006 *m* from the target surface for the case *He*, *Ne*, *Ar* and *Xe* respectively at time $t = 508.0$ *ns*. The limiting characteristic distance (R) for the shock front can be estimated by equating the mass of the gas encompassed by shock wave and initial ablated mass (M_a), that is $R = (3M_a/2\pi\rho_b)^{1/3}$ where ρ_b is the density of background

gas. The estimated distance of the shock front (R) at which the shock wave model is valid for 1.0 *mbar* pressure of *He*, *Ne*, *Ar* and *Xe* are 0.018 *m*, 0.01 *m*, 0.0083 *m* and 0.0057 *m* respectively. Hence our simulation roughly capture the limiting characteristics distance (plume length) for shock wave expansion as shown in Figure 6.

In order to get more insight into the intensity jump at the shock front and its strength in different background gases, the intensity profiles along the expansion axis are analyzed at onset of time.

Variation of intensity/density in the plasma plume at 1 *mbar* pressure and $t = 508.0$ *ns* along the expansion axis (x -axis) and at $y \sim 0.15$ *m* for all the cases of simulation of background gases is shown in Figure 6. The density jump ahead of the plasma plume due to shock wave formation and its delayed appearance with the decrease of the mass of background gas is clearly visible in Figure 6. Also the intense and sharp intensity jump in the simulation of *Xe* background gas in comparison to the *He* background gas reveals that shock strength (reciprocal of shock thickness) is higher in case of heavier background atoms/gas.

Further, simulated results depicted in Figures 2 and 3 are also compared with theoretically predicted shock-front velocity and density. According to the theory, the shock wave parameters especially the shock-front density and shock-front velocity could be determined based on the mass and energy conservation formula as given below:

$$V_s \approx \left(\frac{\gamma + 1}{2} \right) V_a \quad (15)$$

$$\rho_s \approx \left(\frac{\gamma + 1}{\gamma - 1} \right) \rho_b \quad (16)$$

Where V_s and V_a are the shock-front velocity and velocity of the plume during the initial time evolution of the plume respectively. γ is the ratio of specific heats at constant pressure and volume. As, in our simulation we are using the monatomic gas so the value of γ is 1.67. ρ_s and ρ_b are the shock front density and background density respectively. Thus according to the a above formula if massive shock is present in the system then the shock density should be roughly $\sim 4.0\rho_b$ and shock wave velocity, $V_s \sim 1.34V_a$. The simulated density at the shock fronts in the case of *He*, *Ne*, *Ar* and *Xe* are 2.5×10^{-3} , 8.3×10^{-3} , 1.25×10^{-2} and 2.0×10^{-2} respectively in the dimensionless unit (see, Figure 6). In the simulation, the density is normalized by the plume-density ρ_v at $t = 0.0$ that is $\rho_v^{t=0.0} = 1.75$ *kg/m*³. Thus the actual value of density in the shock fronts (at $t = 304.0$ *ns* and at 1 *mbar* pressure) are as follows, $\rho_v^{He} = 4.38 \times 10^{-3}$, $\rho_v^{Ne} = 1.46 \times 10^{-2}$, $\rho_v^{Ar} = 2.2 \times 10^{-2}$ and $\rho_v^{Xe} = 3.5 \times 10^{-2}$ in the unit of *kg/m*³. If one compare these values with its corresponding background gas density that is $\rho_b^{He} \sim 1.6 \times 10^{-4}$ *kg/m*³, $\rho_b^{Ne} \sim 8.1 \times 10^{-4}$, $\rho_b^{Ar} \sim 1.6 \times 10^{-3}$ and $\rho_b^{Xe} \sim 5.3 \times 10^{-3}$ (in the unit of *kg/m*³), the value of shock front density is always greater than ~ 10 times of the background density in all cases of the simulation which is overestimated the theoretical value of the ideal blast wave model.

Further, we estimated the velocity (V_a) of the ablated plume using the relation,

Table 1. Values of α and β , and shock velocity V_s ($\sim 0.4\alpha t^{-0.6}$) in simulations of *He*, *Ar* and *Xe* ambient gases at 1 *mbar* pressure.

| Ambient gas | α | β | V_s (m/s) |
|-------------|-------------------------|--------------------------|--------------------|
| <i>He</i> | 2.6557×10^{-3} | -1.6067×10^{-2} | 2.55×10^4 |
| <i>Ar</i> | 2.1597×10^{-3} | -1.2596×10^{-2} | 2.08×10^4 |
| <i>Xe</i> | 1.7586×10^{-3} | -9.977×10^{-3} | 1.69×10^4 |

$v_v = \left(\frac{\gamma kT}{m_v}\right)^{1/2}$. The obtained value of V_a is $1.1 \times 10^4 \text{ m/s}$. This is the velocity with which plume enter the simulation space in the presence of background gas. Note that plume velocity V_a does not change significantly during the initial time evolution of the plume in the background gas. Later when strong shock present in the system then the average shock velocity V_s is determined using the fitting parameters α and β . α and β are constants, appear in the function $\alpha t^{0.4} + \beta$ (also known as a Taylor Sedov model) that is used to fit the shock front position vs. time curve (see Figure 5). The value of α and β depends upon the mass of the background gas. In the case of the simulation of *Xe* background gas, the estimated shock velocity V_s is $\sim 1.69 \times 10^4 \text{ m/s}$. This value is approximately 1.5 times of the initial plume velocity V_a that is in good agreement with the theoretical approximation ($V_s/V_a = 1.3$). Values of α and β , and shock velocity V_s are summarized in table I for the simulation of all the ambient gases performed at 1 *mbar* pressure.

Another noteworthy observation of the present simulation is that it predict the density discontinuity in between the plasma plume and shock front due to the hydrodynamic movement of plume and shock front as reported by several experimental works in the past. Two region of discontinuity is clearly visible in case of the simulation of the background gases *Ne* and *Ar* as shown in Figure 6. While in the case of the simulation of *Xe* background gas this is not visible due to the nominal separation between the plume and shock-front. Also in the case of the simulation of *He* background gas this discontinuity is not clearly visible, here it is because of the weak-shock condition (see Figure 6). In most of the previous work, the first discontinuity is attributed to the ionized shocked gases just behind the shock front. Whereas the second discontinuity, known as contact surface (CS) which is the boundary of ablated species. Using the Westwood model [37] we can easily understand the change in the direction of carbon species in a single collision with *Ne* and *Ar* background gas species. Thus, elastic scattering between the leading plume species and heavier background atoms play the significant role in the build-up of the density in the CS region.

Apart from the characteristic expansion of the plasma plume and shock wave formation, our simulation also capture the most of the features of lateral interactions between two spatially separated plumes and its dependence on the background conditions (that is pressure and mass of the background gas. The earlier studies report

the formation of well defined interaction region (or stagnation region) in parallel to propagating plasma plumes in close proximity. Due to the angular distribution of the plume species, interaction between the counter propagating plume species with the condition $\eta = \frac{D}{\lambda} \gg 1$, is responsible for the formation of interaction region. Where η , D and λ are respectively, the collisionality parameter, separation between the plumes and collision frequency. For the higher value of η , the counter propagation energetic particles lose energy rapidly due to multiple collisions and formed the interaction region. Thus the value of η define whether the interaction between the plumes result into the interpenetration or it simply turned into the interaction zone (as observed in the simulation).

The one to one comparison between the images observed in different background gas and pressure (as shown in Figures 2 and 3) indicates that dynamics and geometrical structure of the expanding vapour, shock front and interaction zone at 1 *mbar Ne* pressure is nearly similar to the simulated images at 3 *mbar He* pressure. On the same way, the characteristics of the plumes and its interaction pattern at 1 *mbar Xe* pressure resembles that observed at 3 *mbar Ar* pressure. Based on the above observations, the interaction mechanism between the plumes is broadly divided into two region that is in the region where absence or weak shock condition and presence of strong shock front. In absence of shock front, for example at 208 *ns* and 304 *ns* in *He* and at 208 *ns* in *Ne* background at 1 *mbar* pressure (see, figure 2), an additional luminous components in between the plumes in our simulation is treated as conventional interaction region formed by the multiple collisions between the counter propagating species at the middle of two expanding plumes.

The present simulation is also predict the higher expansion velocity of interaction region in comparison to interacting plumes, which is in excellent agreement with previously reported experimental results. Scenario is different in presence of shock wave ahead of plume where shock-shock interaction and subsequent reflections come in picture along with the interaction between plume species. With the assumption of collision between two planner shock fronts, shock-shock interactions and its subsequent reflections is classified as regular and Mach reflections depending upon the shock strength and angle of incidence with respect to the plane of symmetry.

The carefull examination of the simulated images in case of *Ne* and *Ar* at 1 *mbar* pressure and at time delay > 200 *ns* (Figure 2) and also at 3 *mbar* of *He* pressure (Figure 3), It can be clearly seen that shock fronts are physically interact at the middle of the two plumes. In this simulation both plume is identical and therefore point of interaction is always lying in the middle and moving along the expansion axis with time as observed in Figure 2. This good agreement with theoretically predicted interaction and regular reflection of two relatively weak shock fronts. Also the predicted structure of the interaction zone is an excellent agreement with the experimental observation in the similar condition.

On the other hand in case of heavier background gas (*Ar* and *Xe*) and especially at higher pressure and later time delay where the strong shock is predicted, luminous

interaction region is not observed in simulation even at highest considered time delay (see, Figure 3). Also in contrast to the weak shock condition, physical overlapping between the shock fronts is not observed in this region. The density discontinuity in between the plumes is clearly visible in 3 *mbar* pressure of *Ar* and *Xe* at 500 *ns* time delay (Figure 3) where the interacting shock wings is seems to repelled each other and hence completely suppressed in opposite direction. This observation is resembled with the case of Mach reflection between the two interacting strong shock fronts. In this case point of reflection is split into two symmetrical points and move in opposite direction in plane perpendicular to expansion axis. The reflections from these two points restrict the escape of plume species and form the density discontinuity in between the plume as shown in Figure 3.

Interaction between the plumes as well as shock fronts and its dependence on the shock strength is represented in better way by comparing the interactions of plasma plumes in *He* and *Xe* background gases at 3 *mbar* pressure as shown in Figure 4. As discussed earlier, conventional interaction region is observed at ~ 200 *ns* in *He* where the shock front is insignificant. Even at 3 *mbar* *He* pressure, relatively weak shock is predicted in our simulation. Thus the simulated structure of interaction region at $t > 200$ *ns* is in line with the interaction between two weak shock fronts. However the complete suppression of overlapping of plume species and shock wings and hence the formation of interaction zone because of Mach reflection between the strengthen shock front in *Xe* background is correctly predicted in our simulation.

In this simulation we successfully predicted the most of the features of colliding plumes and shock fronts and also the transition from regular to Mach shock reflection in reference of weak and strong shock conditions.

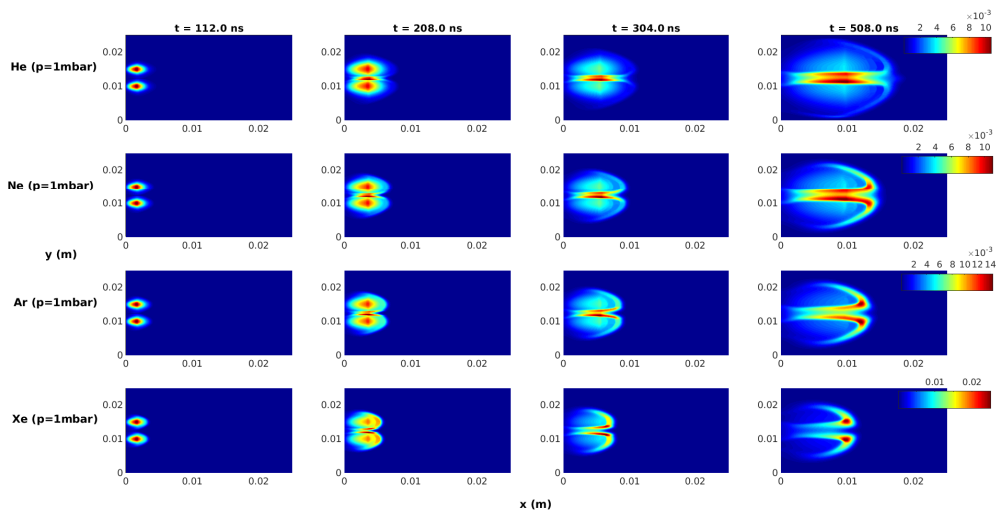


Figure 2. (left to right) Time evolution of two plasma plumes from simulations in the presence of *He*, *Ne*, *Ar* and *Xe* background gases at 1.0 *mbar* pressure; initial separation between plumes is considered 5.0 *mm*.

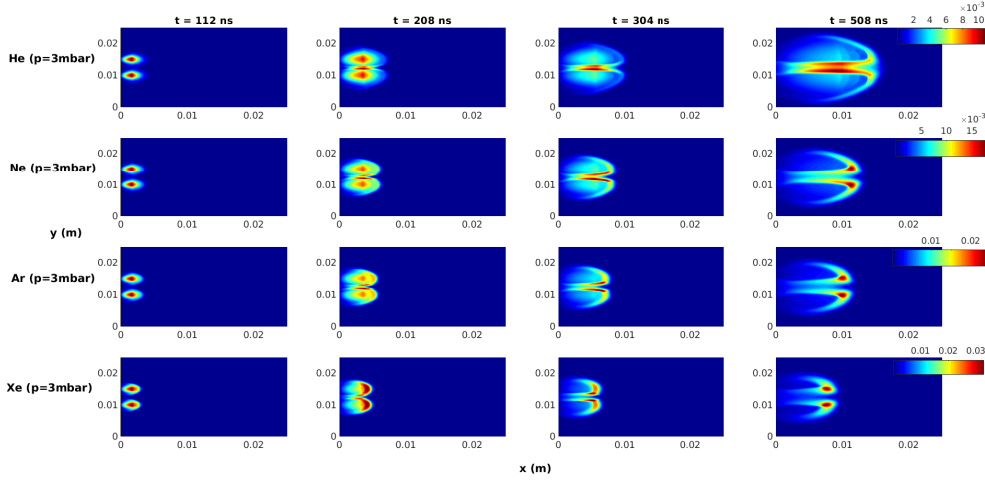


Figure 3. (left to right) Time evolution of two plasma plumes from simulations in the presence of *He*, *Ne*, *Ar* and *Xe* background gases at 3.0 *mbar* pressure; initial separation between plumes is considered 5.0 *mm*.

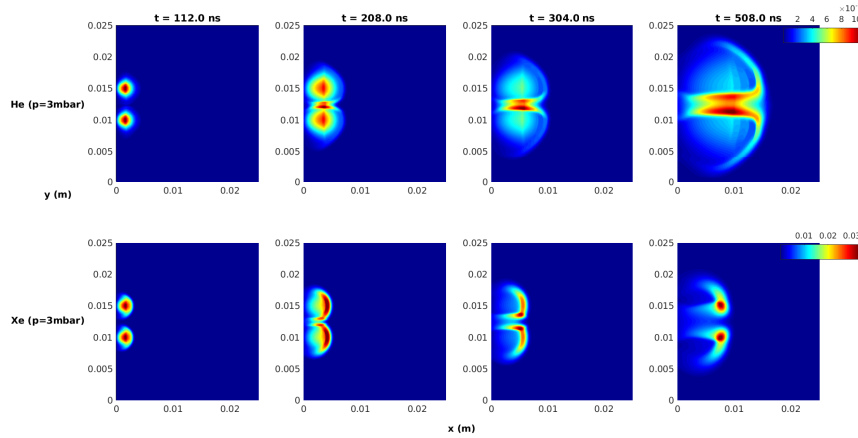


Figure 4. Comparison of the images of the time evolution of plasma plumes from simulations in *He* and *Xe* background gases at 3.0 *mbar* pressure.

4. Conclusion

In this work we presented the numerical simulation of the evolution of two spatially separated plasma plumes in the presence of *He*, *Ne*, *Ar* and *Xe* background gases at 1 and 3 *mbar* pressures. The features of expanding plasma plumes in close proximity and interaction between them in different background gas captured in the present simulation are in close agreement with the reported experimental observations [25]. Effect of mass of ambient gas on plume dynamics, initiation of shock waves, shape and strength of shock front and variation of the density/intensity in the plume as well as shock region is precisely reproduced in the simulation. Further lateral interaction between the

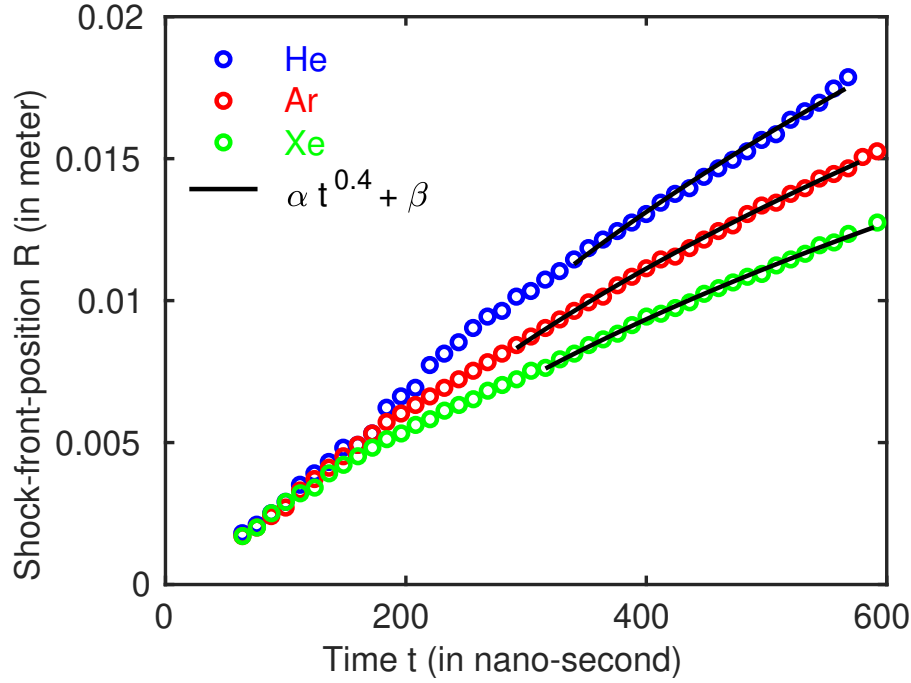


Figure 5. Plot of the shock front position versus time in the simulations of *He*, *Ar* and *Xe* background gases at 1.0 mbar background pressure. Each of them is fitted at later time beyond ~ 300 ns using function, $\alpha t^{0.4} + \beta$ where α and β are the fitting constants, and its value depends upon the background gas and pressure. The value of α and β are summarized in table I.

two expanding plumes and formation of interaction region are also predicted well by the simulations. The structure formation because of the shock-shock interaction and reflection observed in simulation is in good agreement with the experimental results. The observed results suggest the presence of the regular shock-reflection in the cases of the simulation of *He* and *Ne* background gases and Mach-reflection in the cases of *Ar* and *Xe* simulations especially at later time. The simulation in the different ambient gases demonstrate the transition from regular to Mach reflections of shock wave depending upon the shock strength.

References

- [1] M. von Allen and A. Blatter, Laser-Beam Interactions with Materials:Physical Principles and Applications (Springer, Berlin, 1995).
- [2] D. B. Chrisey and G. K. Hubler, Pulsed Laser Deposition of Thin Films (Wiley, New York, 1994).
- [3] Kaushik Choudhury, R.K. Singh, P. Kumar, Mukesh Ranjan, Atul Srivastava and Ajai Kumar, Nano-Structures & Nano-Objects **17**, 129 (2019).
- [4] A. W. Miziolek, V. Pallechi, I. Schechter, Laser Induced Breakdown Spectroscopy (Cambridge University Press, 2006).
- [5] J. R. Freeman, S. S. Harilala), and A. Hassanein, Journal of Applied Physics **110**, 083303 (2011).
- [6] Y. P. Zakharov, IEEE Transactions on Plasma Science **31**, 1243 (2003).
- [7] A. Huber, U. Samm, B. Schweer, and Ph. Mertens, Plasma Phys. Controlled Fusion **47**, 409 (2005).

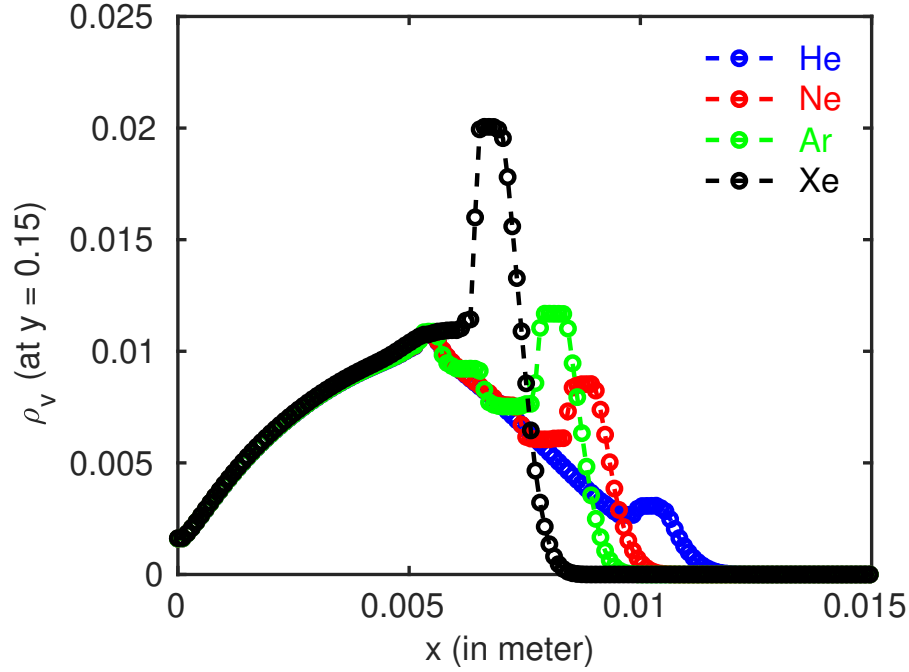


Figure 6. Variation of density (and/or intensity) along x -axis in the upper plume of the image displayed in figure 2 at $t = 500.0$ ns from the simulations of background gases, *He*, *Ne*, *Ar* and *Xe* at 1.0 mbar background pressure. The variation of density is passing through the center of the plume (located at $y = 0.15$ m position).

- [8] P. Hough, C. McLoughlin, S. S. Harilal, J. P. Mosnier and J. T. Costello, *J. Appl. Phys.* **107**, 024904 (2010).
- [9] S. V. Bulanov, T.Z. Esirkepov, F.F. Kamenets, Y. Kato, A.V. Kuznetsov, K. Nishihara, F. Pegoraro, F. Tajima, and V. S. Khoroshokov, *Plasma Phys. Rep.* **28**, 975 (2002).
- [10] O. Rancu, P. Renaudin, C. Chenais-Popovics, H. Kawagashi, J.C. Gauthier, M. Dirksmeoller, T. Missalla, I. Uschmann, E. Forster, O. Larroche, O. Peyrusse, O. Renner, E. Krousky, H. Pepin, and T. Shepard, *Phys. Rev. Lett.* **75**, 3854 (1995).
- [11] A. S. Wan, T. W. Barbee, R. Cauble, P. Celliers, L. B. Da Silva, J. C. Moreno, P. W. Rambo, G. F. Stone, J. E. Trebes, and F. Weber, *Phys. Rev. E* **55**, 6293 (1997).
- [12] C. D. Gregory, J. Howe, B. Loupias, S. Myers, M. M. Notley, Y. Sakawa, A. Oya, R. Kodama, M. Koenig, and N. C. Woolsey, *Astrophys. J.* **676**, 420 (2008).
- [13] Y. Kuramitsu, Y. Sakawa, T. Morita, C. D. Gregory, J. N. Waugh, S. Dono, H. Aoki, H. Tanji, M. Koenig, N. Woolsey, and H. Takabe, *Phys. Rev. Lett.* **106**, 175002 (2011).
- [14] R. C. Elton, D. M. Billings, C. K. Manka, H. R. Griem, J. Grun, B. H. Ripin, and J. Resnick, *Phys. Rev. E* **49**, 15121519 (1994).
- [15] J. Dardis, J.T. Costello, *Spectrochimica Acta Part B* **65**, 627 (2010).
- [16] K. F. Al-Shboul, S. S. Harilal, S. M. Hassan, A. Hassanein, J. T. Costello, T. Yabuuchi, K. A. Tanaka, and Y. Hirooka, *Phys. Plasmas* **21**, 013502 (2014).
- [17] C. Sánchez Aké, R. Sanginés de Castro, H. Sobral and M. Villagrán-Muniz. *J. Appl. Phys.* **100**, 053305 (2006).
- [18] S. S. Harilal, M. P. Polek, and A. Hassanein, *IEEE Trans. Plasma Sci.* **39**, 2780 (2011).
- [19] R. T. Eagleton, J. M. Foster, P. A. Rosen, and P. Graham, *Rev. Sci. Instrum.* **68**, 834 (1997).
- [20] H. Luna, K. D. Kavanagh, and J. T. Costello, *J. Appl. Phys.* **101**, 033302 (2007).
- [21] Bhupesh Kumar, R. K. Singh, Sudip Sengupta, P. K. Kaw, and Ajai Kumar, *Phys. Plasmas* **21**, 083510 (2014).

- [22] E. Camps, L. Escobar-Alarcn, E. Haro-Poniatowski, M. Fernndez-Guasti, Appl. Surface Sci. **9**, 239 (2002).
- [23] Y. Hirooka, T. Oishi, H. Sato, and K. A. Tanaka, Fusion Sci. Technol. **60**, 804 (2011).
- [24] Bhupesh Kumar, R. K. Singh, Sudip Sengupta, P. K. Kaw, and Ajai Kumar, Phys. Plasmas **22**, 063505 (2015).
- [25] Bhupesh Kumar, R. K. Singh, Sudip Sengupta, P. K. Kaw, and Ajai Kumar, Phys. Plasmas **23**, 043517 (2016).
- [26] R. K. Singh, Ajai Kumar, B. G. Patel and K. P. Subramanian, J. Appl. Phys. **101**, 103301 (2007).
- [27] Y. T. Lie, A. Pospieszczyk, and J. A. Tagle, Fusion Technol. **6**, 447 (1984).
- [28] A. Pospieszczyk, F. Aumayr, E. Hintz, and B. Schweer, J. Nucl. Mater. **574**, 162164, (1989).
- [29] W. K. Kumuduni, Y. Nakayama, Y. Nakata, T. Okada and M. Maeda, J. Appl. Phys. **74**, 7510 (1993).
- [30] Sony George, R.K. Singh, V.P.N. Nampoori and Ajai Kumar, Physics Letters A **377**, 391 (2013).
- [31] Y. B. Zeldovich and Y.P. Raizer, Physics of Shock Wavesand High Temperature Hydrodynamic Phenomena (NewYork: Dover, 2002).
- [32] Sharad K Yadav, Bhavesh G Patel, R. K. Singh, Amita Das, Predhiman K Kaw and Ajai Kumar, J. Phys. D: Appl. Phys. **50**, 355201 (2017).
- [33] Bhavesh G. Patel, Amita Das, Predhiman Kaw, Rajesh Singh, and Ajai Kumar, Phys. Plasmas **19**, 073105 (2012).
- [34] R. B. Bird, W. E. Stewart, and E. N. Lightfoor, *Transport Phenomena* (Wiley 2006).
- [35] A. Bogaerts, Z. Chen, R. Gijbels, and A. Vertes, Laser ablation for analytical sampling: what we can learn from the modelling ? Spectrochem. Acta. Part B **58 (11)**, 1867-1893 (2003).
- [36] J. P. Boris, A. M. Landsberg, E. S. Oran, and J. H. Gardner, "LCPFCT-Flux-corrected transport algorithm for solving generalized continuity equations" *Technical Report No. NRL/MR/6410-93-7192* Naval Research Laboratory, 1993.
- [37] W. D. Westwood, Journal of Vacuum Science & Technology **15**, 1 (1978).